

## SH WAVE SCATTERING BY A NANOCRACK IN A GRADED PIEZOELECTRIC HALF-PLANE WITH NANORELIEF

TSVIATKO V. RANGELOV<sup>1\*</sup>, PETIA S. DINEVA<sup>2</sup>

<sup>1</sup>*Institute of Mathematics and Informatics, Bulgarian Academy of Sciences, Sofia 1113, Bulgaria*

<sup>2</sup>*Institute of Mechanics, Bulgarian Academy of Sciences, Sofia 1113, Bulgaria*

[Received: 17 January 2025. Accepted: 30 September 2025]

doi: <https://doi.org/10.55787/jtams.25.55.3.343>

**ABSTRACT:** The study focuses on an exponentially graded piezoelectric (PEM) half-plane featuring a nanorelief along its surface boundary, which also includes a blunt nanocrack. The system is subjected to anti-plane time-harmonic elastic SH waves propagating at an incident angle in the nano half-plane. The model integrates the continuum mechanics approach with the Gurtin-Murdoch surface elasticity model. An efficient, non-hypersingular traction boundary integral equation method (BIEM) is developed, verified, and applied in simulation studies. This method is based on an analytically derived Green's function for a graded PEM half-plane. A parametric study illustrates the significant influence of factors such as material gradient magnitude, surface elasticity, nanorelief and nanocrack characteristics on the generalized stress concentration factors (GSCFs).

**KEY WORDS:** PEM graded half-plane, nanorelief, nanocrack, Gurtin-Murdoch model, BIEM, dynamic GSCF.

### 1 INTRODUCTION

The scattering of elastic waves in solids is widely recognized to be influenced by surface roughness [1]. Variations in scattering amplitude, intensity, and their angular distribution are generally understood to depend on both surface characteristics and wave frequency, and this is truth also for multifunctional materials at macro and micro/nano scale. It is well known that the properties of piezoelectric nanomaterials are size-dependent, as demonstrated by numerous experimental studies. Some of these results show that:

- (a) The Young's modulus of ZnO nanowires increases from 140 GPa to 160 GPa as the nanowire diameter decreases from 80 nm to 20 nm [2];

---

\*Corresponding author e-mail: [rangelov@math.bas.bg](mailto:rangelov@math.bas.bg)

- (b) The fracture strength of ZnO nanowires increases with decreasing nanowire diameter [3];
- (c) The piezoelectric constants of GaN nanowires have been reported to be up to six times higher than their bulk values [4].

The absence of an intrinsic length scale  $h$  in the constitutive laws of classical continuum mechanics prevents it from capturing the size-dependent behavior of solids. A categorization of nanomechanical models based on the relationship between material microstructure and the intrinsic length scale is discussed in [5]. Continuum mechanics-based models for nano-objects are based on the non-local elasticity, strain gradient theory and surface elasticity model of [6]. In the latter model, the surface is treated as a thin layer of negligible thickness that is perfectly adhered to the underlying bulk material without slipping. The surface properties and constitutive relations differ from those of the bulk material.

Despite having zero thickness, the surface layer  $S$  is elastic and isotropic, with its own surface Lamé constant  $\mu_S$ . Its local constitutive law, expressed in the tangential direction  $l$ , is given by  $\sigma_{ll}^S = \mu^S \varepsilon_{ll}^S$ , where  $\sigma_{ll}^S$  and  $\varepsilon_{ll}^S$  represent the tangential stress and strain, respectively. Under the Gurtin-Murdoch theory, the conventional boundary conditions along the surface layer  $S$  are replaced by non-classical boundary conditions that incorporate the unique surface elasticity effects. Meanwhile, the bulk material continues to be described by classical continuum mechanics.

A detail review on the mechanical models describing dynamic behavior of nanocracked heterogeneous and inhomogeneous infinite, semi-infinite and finite PEM solids without surface relief is presented by the authors in [7–12]. Based on the state-of-the-art analysis in these authors' publications, several conclusions can be drawn:

- There is a notable lack of research addressing anti-plane dynamic problems in homogeneous and graded piezoelectric solids with nanocracks;
- Despite the well-known advantages of the BIEM, its application as an effective numerical technique in the fracture mechanics of piezoelectric nanocomposites remains limited;
- There is a limited number of studies addressing surface elasticity effects on stresses near the crack tip, with most focusing on static loads.

To the best of the authors' knowledge, there is a lack of results in the dynamic fracture mechanics of functionally graded nanocracked piezoelectric nanocomposites. In the limited number of studies in this research area, none have considered solids with boundaries featuring nanocanyon.

The aim of this paper is to develop a new mechanical model that describes the dynamic stress field near the crack tips of a blunt nanocrack, subjected to an incident time-harmonic SH wave propagating in an anisotropic piezoelectric semi-infinite solid with a surface nanocanyon along its boundary. This model is incorporated into a parametric study using the BIEM, accounting for the surface elasticity effect through the Gurtin-Murdoch model.

The paper is organized as follows: Sections 2 and 3 present the statement of the problem and its reformulation using BIEM, respectively, followed by a series of numerical results in Section 4. A discussion and conclusions are provided in Section 5.

## 2 PROBLEM FORMULATION

The dynamic behaviour of an exponentially graded in depth transversely isotropic piezoelectric half-plane (Fig. 1) is studied. We consider two type of reliefs embedded in the half-plane. The first has the shape of a semi-ellipse with major semi-axes  $a$  and minor semi-axes  $b$ ,  $b \leq a$ , see Fig. 1a. This shape, denoted as  $\Gamma_{r_1}$  features a single valley. The second relief is formed by continuously moving the point with coordinates  $(0, b)$  along the  $Ox_2$ -axis, resulting in a shape with two consecutive valleys (see Fig. 1b). This shape is denoted as  $\Gamma_{r_2}$ . These two types of reliefs serve as model examples for numerical studies. Figures 3 – 7 concern relief  $\Gamma_{r_1}$ , while Figs. 9 and 10 correspond to relief  $\Gamma_{r_2}$ .

Our aim is to show the applicability of the developed and verified BIEM in the graded nanocracked half-plane with nanorelief by using the Green's function. Note that in the numerical solutions of BIEM we will approximate  $\Gamma_{r_1}$ ,  $\Gamma_{r_2}$  with linear segments. The curvature at the mid point of the corresponding arc is used in the new boundary conditions Eq. (2) taking into account the surface effect. Although linear segments are used to illustrate the relief boundary, the mesh itself consists of 7 quadratic boundary elements. For each figure related to the nanorelief, a preliminary convergence study was conducted by comparing results obtained with different numbers of boundary elements along the nanorelief boundary. The results demonstrate that using 7 boundary elements provides sufficient accuracy and ensures convergence of the solution. The boundary element method software developed by the authors has been verified through the analysis of various dynamic fracture problems in PEM. Extensive discussions regarding the accuracy and convergence of the developed methodology can be found in several of the authors' publications; see [7, 13].

The boundary  $\Gamma_f = \Gamma_{ff} \cup \Gamma_r$ , consists of a flat boundary part  $\Gamma_{ff}$  and nanorelief boundary:  $\Gamma_r = \Gamma_{r_1}$  in Fig. 1a or  $\Gamma_r = \Gamma_{r_2}$  in Fig. 1b. The half-plane contains a vertical or horizontal nanocrack  $\Gamma_c$ , an open segment with length  $2c$  which is subjected to incident time-harmonic elastic SH wave with a fixed frequency  $\omega$  and incident angle  $\theta$ . Anti-plane wave motion in a plane  $x_3 = 0$  of a Cartesian coordinate sys-

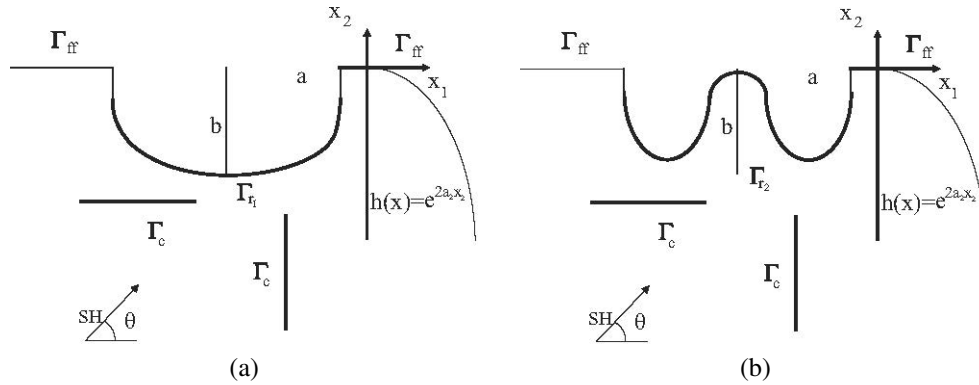


Fig. 1. Problem geometry: (a) horizontal; and (b) vertical nanocrack in a graded PEM half-plane with surface nanorelief.

tem  $Ox_1x_2x_3$  is considered. PEM shows hexagonal symmetry with respect to the axis  $Ox_3$  and the poling axis is collinear with it. The nanocrack is modelled as a blunt one with a root in the shape of a semi-ellipse, with semi-major and semi-minor axes denoted as  $c_0$  and  $c_1$ , respectively, see Fig. 2. The perimeter of the crack is  $|S| = 2(2c - 2c_0) + 4c_0E(e)$ ,  $c_0 = 0.0375c$ , with a size  $c$  belonging to the interval  $10^{-7} \text{ m} - 10^{-10} \text{ m}$ ,  $E(e) = \int_0^{\pi/2} \sqrt{1 - e^2 \sin^2 \varphi} d\varphi$  is a complete elliptic integral of second kind and  $e = \sqrt{1 - (c_1/c_0)^2}$ , see [14]. If  $c_1 = c_0$  the blunt nano-crack is with a crack's root presented by semi-circular shape of radius  $c_0$ . If  $c_1 = 0$ , the blunt nanocrack degenerates to a line crack with length  $2c$ . The inhomogeneity function

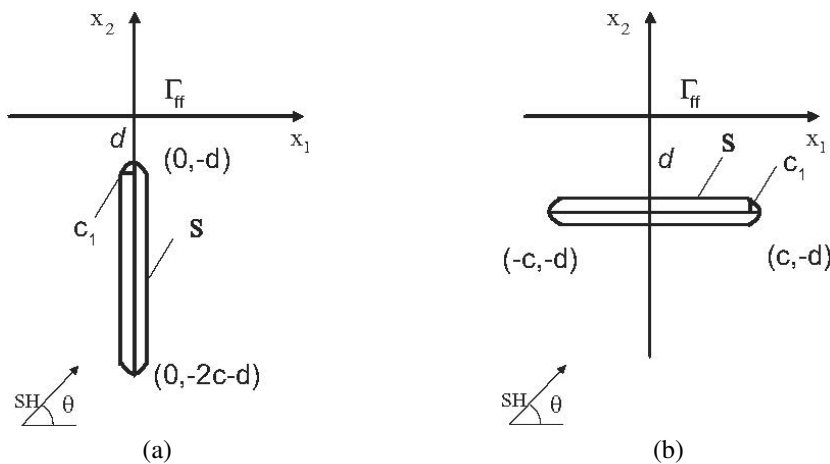


Fig. 2. Blunt nanocrack model: (a) vertical; (b) horizontal.

for exponentially graded material is  $h(x) = e^{2a_2x_2}$ , where  $a_2$  is the coefficient of the material gradient. The material properties are as follows: elastic stiffness variable  $c_{44}(x) = c_{44}^0 h(x)$ , piezoelectric variable  $e_{15}(x) = e_{15}^0 h(x)$ , dielectric variable  $\varepsilon_{11}(x) = \varepsilon_{11}^0 h(x)$  and density  $\rho(x) = \rho^0 h(x)$  and  $c_{44}^0, e_{15}^0, \varepsilon_{11}^0, \rho^0$  are reference material constants. Note that in this study we will consider only the case of wave propagation, i.e., the wave number is  $k^2 = \rho^0 \omega^2 / \gamma - a_2^2 > 0$ ,  $\gamma = c_{44}^0 + e_{15}^{02} / \varepsilon_{11}^0$ , see [13].

The only non-zero field quantities dependent on coordinates  $x = (x_1, x_2)$  and  $\omega$  are:

- mechanical field variables: displacement component  $u_3(x, \omega)$ ; stress tensor components  $\sigma_{13}(x, \omega), \sigma_{23}(x, \omega)$ ; strain components  $s_{13}(x, \omega), s_{23}(x, \omega)$ ;
- electrical field variables: electric field components  $E_1(x, \omega), E_2(x, \omega)$ , electrical displacements  $D_1(x, \omega), D_2(x, \omega)$  and electrical potential  $\phi(x, \omega)$ .

The following generalized notations for the displacement and stress are used:

$$u_J = \begin{cases} u_3, & J = 3 \\ \phi, & J = 4 \end{cases}, \quad \sigma_{iJ} = \begin{cases} \sigma_{ij}, & J = 3, i = 1, 2 \\ D_i, & J = 4, i = 1, 2 \end{cases}.$$

We define the following governing equations:

- The constitutive equation is

$$\sigma_{iJ} = C_{iJKl}(x)u_{K,l} = C_{iJKl}(x)s_{Kl},$$

where  $i, l = 1, 2$  and

$$C_{i33l} = \begin{cases} c_{44}, & i = l \\ 0, & i \neq l \end{cases}; \quad C_{i34l} = \begin{cases} e_{15}, & i = l \\ 0, & i \neq l \end{cases}; \quad C_{i44l} = \begin{cases} -\varepsilon_{11}, & i = l \\ 0, & i \neq l \end{cases}.$$

Note that  $C_{iJKl}(x) = C_{iJKl}^0 h(x)$ , where  $C_{iJKl}^0$  are the reference material properties;

- The elastic strain-displacement and the electrical field-potential kinematic relations are  $s_{i3} = u_{3,i}$  and  $E_i = -\phi_{,i}$ ;
- The mechanical and electrical balance equation for time-harmonic processes in absence of body forces and free electric charges is

$$(1) \quad \sigma_{iJ,i} + \rho_{JK}\omega^2 u_K = 0, \quad \rho_{JK} = \begin{cases} \rho, & J = K = 3 \\ 0, & J = 4 \text{ or } K = 4 \end{cases}.$$

Note that in the time domain the electric field generated in piezoelectrics can be assumed to be quasi-static, as the velocity of the elastic wave is much smaller than that of the electromagnetic wave. Therefore, the magnetic field generated by the elastic waves is negligible. This implies that the time derivative of the magnetic field  $B(x, t)$  is approximately zero, i.e.  $\frac{\partial B(x, t)}{\partial t} \approx 0$ . Thus one of Maxwell's equations of electrodynamics becomes  $\text{rot}E(x, t) = \frac{\partial B(x, t)}{\partial t} \approx 0$ , hence  $E(x, t) = -\text{grad}\phi(x, t)$ . Consequently, a piezoelectric continuum is based on the governing equations of elastodynamics assuming small deformations and quasi-electrostatic fields.

The following assumptions are made:

- (a) the bulk material is transversely isotropic PEM;
- (b) the interface  $\Gamma_c$  between the nanocrack and PEM matrix and between the nanorelief  $\Gamma_r$  and the matrix is considered as an infinitely thin elastic isotropic layer with own surface elastic shear coefficient  $\mu^S$ . The following constitutive equation is satisfied along this infinitely thin layer

$$\sigma_{l3}^S = \mu^S s_{l3}^S = \mu^S \frac{\partial u_3^S}{\partial l},$$

here  $l$  is the tangential vector along the interface under consideration,  $s_{l3}^S$  and  $u_3^S$  are the tangential mechanical deformation and tangential mechanical displacement component;

- (c) the infinitely thin interface layers  $\Gamma_c$  and  $\Gamma_r$  are coherent and the surface mechanical strain in tangential direction with respect to the interface boundary is equal to the associated tangential strain inside the matrix, i.e.  $s_{l3}^S = s_{l3}^M$ ;
- (d) the nanocrack boundary  $\Gamma_c$  and the boundary  $\Gamma_{ff} \cup \Gamma_r$  are assumed to be electrically impermeable and in this case the boundary conditions for the normal component of the electric displacement is  $D_n = 0$ .

Having in mind these assumptions, the boundary condition for the mechanical stress satisfies the non-classical boundary condition, derived in the frame of [6] model and they are

$$(2) \quad t_3(x, \omega) = \sigma_{13}(x, \omega)n_1 + \sigma_{23}(x, \omega)n_2 = -\frac{\partial \sigma_{13}^S}{\partial l} = -\mu^S \frac{\partial^2 u_3^S(x, \omega)}{\partial l^2},$$

where  $n = (n_1, n_2)$  is the outward pointing unit normal vector to the surface under consideration.

The boundary condition for the mechanical traction along the boundary  $\Gamma_{ff}$  is:

$$(3) \quad t_3(x, \omega) = 0.$$

The total generalized displacement  $u_J(x, \omega)$  and generalized stress  $\sigma_{iJ}(x, \omega)$  in the half-plane wave field is a sum of the generalized free-field motion solution for displacement  $u_J^{ff}$  and for the stress  $\sigma_{iJ}^{ff}$  and the generalized scattered displacement  $u_J^{sc}$  and the generalized scattered stress  $\sigma_{iJ}^{sc}$ , i.e.,

$$u_J = u_J^{ff} + u_J^{sc} \text{ and } \sigma_{iJ} = \sigma_{iJ}^{ff} + \sigma_{iJ}^{sc}.$$

The free-field wave motion solution satisfies equation of motion Eq. (1), traction-free boundary condition Eq. (3) along the boundary of the half-plane without any relief and nanocracks and Sommerfeld's radiation condition at infinite.

The free-field motion wave solution for generalized displacements in an exponentially graded half-plane under incident SH-wave is derived analytically in [15] and shown in the Appendix.

The boundary value problem (BVP) describing the formulated above mechanical problem is presented by governing Eq. (1), the boundary condition Eq. (2) along the boundary  $\Gamma_c \cup \Gamma_r$ , the traction free boundary condition Eq. (3) on  $\Gamma_{ff}$ , the boundary conditions for an electrically impermeable crack on  $\Gamma_c$ , and Sommerfeld's radiation condition at infinity.

The normalized stress concentration factor (SCF)  $F_{III}^*$  and normalized electrical field concentration factor (EFCF)  $F_E^*$  for a horizontal blunt nanocrack embedded at a depth  $d^*$  and measured at the crack-tip  $(x_1, -d^*), d^* > a, x_1 \rightarrow \pm c$  are evaluated by the formulae:

$$(4) \quad \begin{aligned} F_{III}^*((x_1, -d^*), \omega) &= \lim_{x_1 \rightarrow \pm c} \frac{t_3((x_1, -d^*), \omega)}{t_3^{ff}((x_1, -d^*), \omega) \sqrt{\pi c}} \sqrt{2\pi(x_1 \pm c)}, \quad |x_1| > c, \\ F_E^*((x_1, -d^*), \omega) &= \lim_{x_1 \rightarrow \pm c} e_{15}^0 \frac{E_n(x_1, -d^*), \omega}{t_3^{ff}((x_1, -d^*), \omega) \sqrt{\pi c}} \sqrt{2\pi(x_1 \pm c)}, \quad |x_1| > c, \end{aligned}$$

where:  $t_3^{ff}$  is the mechanical load amplitude on the nanocrack. In the case of normal incident wave  $E_n = E_2 = \frac{-e_{15}^0 t_3 + c_{44}^0 t_4}{e_{15}^0 + c_{44}^0 \epsilon_{11}^0}$ , where  $t_J = \sigma_{iJ} n_i$ .

The aim of the study is to evaluate the sensitivity of the generalized stress concentration wave fields to various factors, including the characteristics of the dynamic load, the crack's surface elasticity properties, the coupled material characteristics, the nanocrack existence and location, the properties of the material gradient, as well as the geometry of the nanorelief and its surface elasticity.

### 3 PROBLEM REFORMULATION VIA BOUNDARY INTEGRAL EQUATIONS

The above formulated BVP is here reformulated by equivalent integro-differential equation along the existing boundary  $\Gamma = \Gamma_c \cup \Gamma_r$ . In the case of cracks the displacement boundary integral equation (BIE) degenerate and due to this the authors develop for the case of graded cracked continuum the method of non-hypersingular traction BIE based on the two-state conservation integral of elastodynamics, see [13]. Note that the system of derived boundary integro-differential equations takes into account the non-classical boundary condition in the developed by [6] model along the nanocrack surface

$$(5) \quad \gamma_{RJ}(x)(t_R^{\text{ff}}(x, \omega) - t_R^M(x, \omega)) \\ = C_{iJKl}(x)n_i(x) \int_{\Gamma} \left[ \left( \sigma_{\eta PK}^g(x, y, \omega) u_{P, \eta}^{\text{sc}, k}(y, \omega) \right. \right. \\ \left. \left. - \rho_{QP} \omega^2 g_{QK}(x, y, \omega) u_P^{\text{sc}, k}(y, \omega) \right) \delta_{\lambda l} \right. \\ \left. - \sigma_{\lambda PK}^g(x, y, \omega) u_{P, l}^{\text{sc}, k}(y, \omega) \right] n_{\lambda}(y) d\Gamma, \quad x \in \Gamma.$$

Here  $\gamma_{RJ}(x)$ ,  $R, J = 3, 4$  is the jump term depending on the local geometry at source point  $x \in \Gamma$ ,  $y \in \Gamma$  is the running point,  $g_{PK}(x, y, \omega)$  is the Green's function of Eq. (1) with Dirac delta at the right hand side,  $\sigma_{iJM}^g(x, y, \omega)$  is its corresponding stress,  $n_i(x)$  are components of the unit outward normal vector to  $\Gamma$ ,  $u_J^{\text{sc}}(y, \omega) = u_J(y, \omega) - u_J^{\text{ff}}(y, \omega)$ . The Green's function for an exponentially graded half-plane, is derived in [15] and shown in the Appendix.

The BVP under consideration is presented now by boundary integral equation (5) and the boundary conditions discussed in Section 2. Note, that this boundary integral equation is based on the analytically derived Green's function for a graded PEM half-plane. Thanks to that the mesh along the flat part of the half-plane surface is avoided as far as the inserted Green's function satisfies the traction-free boundary condition there. Once the solution of BIE (5) is known for a fixed frequency  $\omega$ , the displacement and traction produced by the scattered wave field and by this the total wave field in the piezoelectric half-plane can be obtained via the known representation formulae, see [13].

### 4 NUMERICAL RESULTS

In the numerical scheme proposed, the displacement and traction are approximated with parabolic shape functions and after discretization of the non-hypersingular traction BIEs (5) an algebraic system of equations in respect to the unknowns is obtained and solved, see [13].

The available in the literature results show that for real nanomaterials, the value of  $\mu^S$  is in the neighborhood of  $\pm 10$  N/m, and negative values are also possible, see [16]. Here, in our numerical results, is used the following value of the surface elasticity coefficient  $\mu^S = \pm 6.091$  N/m. The following dimensionless parameters, used in all the numerical examples, are introduced:

- Dimensionless surface parameter on the nanocrack is defined as  $s_{cr} = \frac{\mu^S}{2c_{44}^0 c_1}$ . The parameter  $c_1$  is the curvature radius in the quarter point - boundary elements used for adequately modelling of the crack-tip zones. The radius of curvature  $c_1$  increases proportionally as the blunt nanocrack approaches the line crack geometry. Note, that dimensionless parameter  $s_{cr}$  is introduced to better gauge interface effects at the nanoscale. More specifically, a macroscopic blunt crack with large size  $c_1$  leads to values  $s_{cr} \ll 1$ , and surface effects can be neglected. In opposite, when this value shrinks to the nanoscale, then  $s_{cr}$  becomes noticeable and the surface effect should be taken into account. Dimensionless surface parameter on the nanorelief is defined as  $s_r = \frac{\mu^S}{2c_{44}^0 k_s}$ , where  $k_s$  is the radius of curvature taken at the mid-point of the approximation of nanorelief with linear segments;
- Non-dimesional frequency defined as  $\Omega = c\omega\sqrt{\rho^0 a_0^{-1}}$ ,  $a_0 = c_{44}^0 + \frac{e^{02}}{\varepsilon_{11}^0}$ ;
- Normalized inhomogeneity magnitude  $\beta = 2c|a_2|$ .

The reference mechanical properties of the piezoelectric ceramic material of the type PZT-4 are used in all numerical examples, see Table 1.

The applied discretization mesh consists of 14 quadratic boundary elements along the blunt nanocrack and 7 quadratic boundary elements along the relief boundary, in case of 1a and 1b. The developed and verified numerical procedure is implemented

Table 1. Material properties of piezoelectric ceramic material

Material	Elastic stiffness ( $10^{10}$ N/m <sup>2</sup> )	Piezoelectric coefficient (C/m <sup>2</sup> )	Dielectric constant ( $10^{-10}$ C/Vm)	Density ( $10^3$ kg/m <sup>3</sup> )
	$c_{44}$	$e_{15}$	$\varepsilon_{11}$	$\rho$
PZT-4	2.56	12.7	63.3	7.5

by Mathematica 6, see [17] software package. The accuracy and convergence characteristics of the proposed methodology are checked by keeping the well-known discretization rule of  $\lambda_{SH} > 10l_{BE}$ , where  $\lambda_{SH}$  is the SH-wave length and  $l_{BE}$  is the maximal size of the boundary element in the applied discretization mesh.

#### 4.1 NUMERICAL SCHEME VERIFICATION

To the best of our knowledge, no results are currently available for SH-wave scattering by nanocracks in an exponentially graded piezoelectric material half-plane, with or without surface relief. Therefore, the proposed numerical scheme is verified using a reference test example of a line macro-crack in a homogeneous PEM plane subjected to an incident normal SH-wave. This problem was solved using the singular integral equation method by Wang and Meguid [18].

Specifically, we consider a horizontal or vertical line crack of length  $2c$ , embedded at various depths in a functionally graded PEM half-plane with an inhomogeneity function  $h(x) = 1$ . A comparison between the solution of the reference problem and the authors' solutions for a horizontal or vertical line crack embedded at different depths in the PEM half-plane, is presented in Fig. 3. The authors' solutions are obtained using the numerical scheme discussed above for a graded piezoelectric solid with zero inhomogeneity magnitude. This figure illustrates the well-known observation that, as the embedment depth of the crack  $d$  increases, the wave field in the half-plane converges to the wave field in a full plane. This occurs because the influence of the half-plane's boundary diminishes and becomes negligible. More details for study of the accuracy and convergence of the described numerical scheme can be found in [7, 19].

#### 4.2 PARAMETRIC STUDY

A set of numerical results for a blunt nanocrack in a graded piezoelectric half-plane under incident elastic SH wave is presented highlighting the dependence of the dynamic stress concentration field on the key model parameters such as:

- (a) the wave characteristics-frequency and propagation direction;
- (b) the surface elasticity properties of the nanocrack and the nanorelief;
- (c) the properties of the material gradient;
- (d) the nanocrack-size and position in the half-plane;
- (e) the nanorelief's shape;
- (f) the wave-crack, the crack-relief and the crack-relief-solid's boundary interactions.

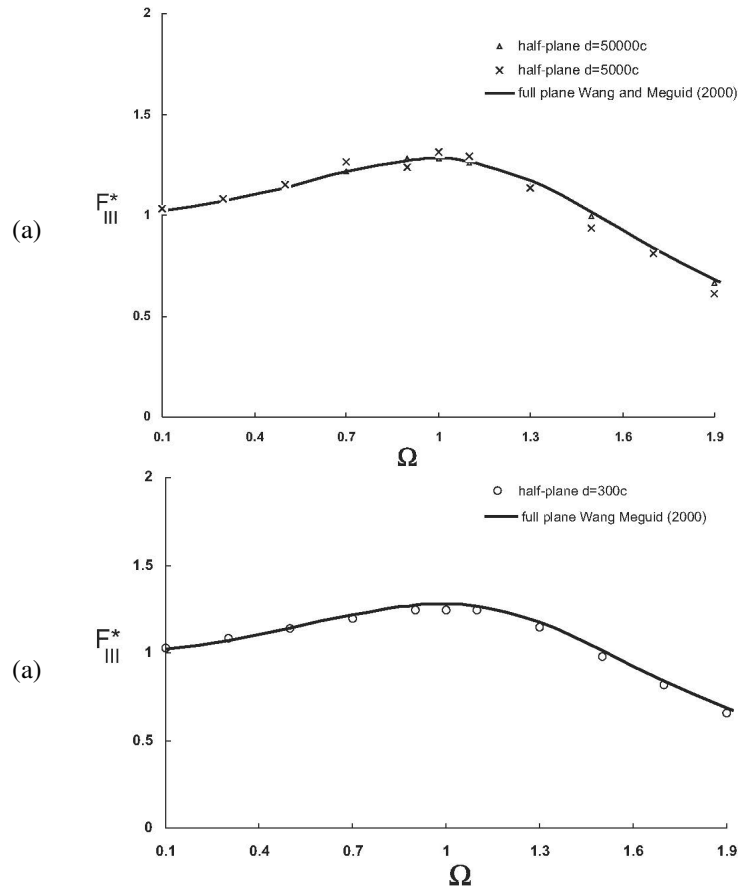


Fig. 3.  $F_{III}^*$  at a crack-tip of a nanocrack without surface effects ( $\mu^S = 0$ ) in a graded with  $\beta = 0.0001$  PEM half-plane versus normalized frequency  $\Omega$ : (a) at the left crack-tip of a horizontal line nanocrack under SH wave with incident angle  $\theta = \pi/2$ ; (b) at the upper crack-tip of a vertical line nanocrack under SH wave with incident angle  $\theta = 0.0001$ .

The sensitivity of the stress concentration field to the embedded nanocrack depth  $d$ , incident wave angle  $\theta$ , and observer location is illustrated in Fig. 4. The model parameters are fixed as follows: wave frequency  $\Omega = 1.3$ , inhomogeneity magnitude of exponentially graded half-plane is  $\beta = 0.2$ , surface elasticity coefficients of the nanorelief  $s_r = 0$  and surface elasticity of the nanocrack  $s_{cr} = 0.02$ . This figure shows normalized SCF  $F_{III}^*$  at different crack-tips of a nanocrack embedded at different depths  $d_2 = 2a + b$ ,  $d_{10} = 10a + b$ ,  $d_{50} = 50a + b$ . The half-plane has a semi-elliptic nanorelief with semi-axes  $a$  and  $b = 0.5a$ . It is subjected to SH-wave with variable incident angle  $\theta = m\pi/20$ ,  $m = 0.0001, 1, \dots, 10$ . Figures 4a,b con-

cern the left and right crack-tips of a horizontal nanocrack, while Figs. 4c, d are for the left (upper) and right (lower) crack-tips of a vertical nanocrack.

The following conclusions can be drawn from the results in Fig. 4:

- The maximum amplitudes of the SCF are strongly influenced by the crack-tip position (upper or lower) in the case of a vertical nanocrack, as seen when comparing Fig. 4c and Fig. 4d. This is not the case for a horizontal nanocrack, as shown in Fig. 4a and Fig. 4b;
- The maximum SCF amplitudes are significantly affected by the depth of the embedded nanocrack, with a common trend observed: the SCF decreases as

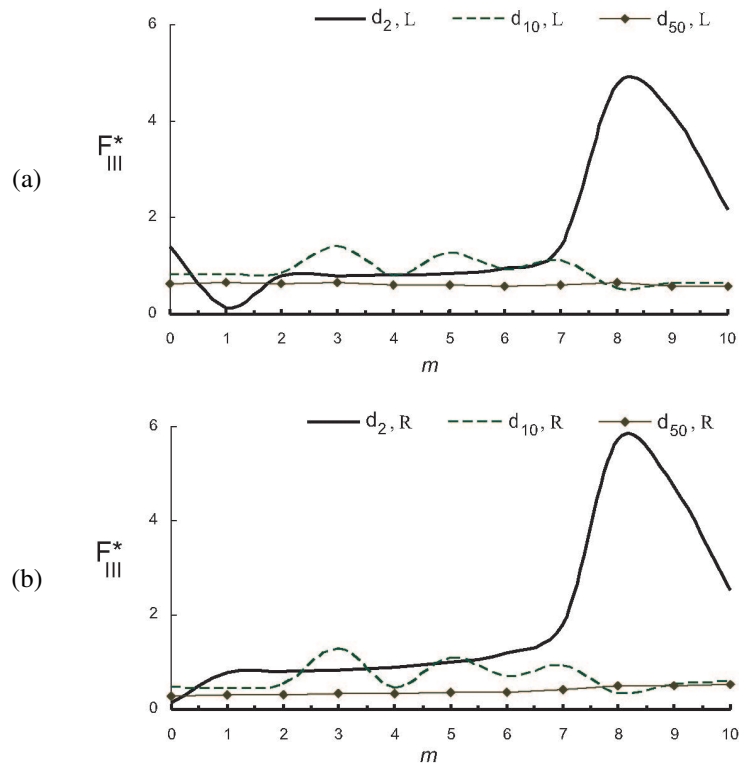


Fig. 4. Normalized SCF  $F_{III}^*$  at different crack-tips of a nanocrack embedded at different depths in an exponentially graded half-plane having a semi-elliptic with semi-axes  $a$  and  $b$  nanorelief  $\Gamma_{r_1}$  under SH-wave with frequency  $\Omega = 1.3$  and incident angle  $\theta = m\pi/20$ ,  $m = 0.0001, 1, \dots, 10$ : (a) left crack-tip L of a horizontal nanocrack; (b) right crack-tip R of a horizontal nanocrack; (c) left (upper) crack-tip L of a vertical nanocrack; (d) right (lower) crack-tip R of a vertical nanocrack.

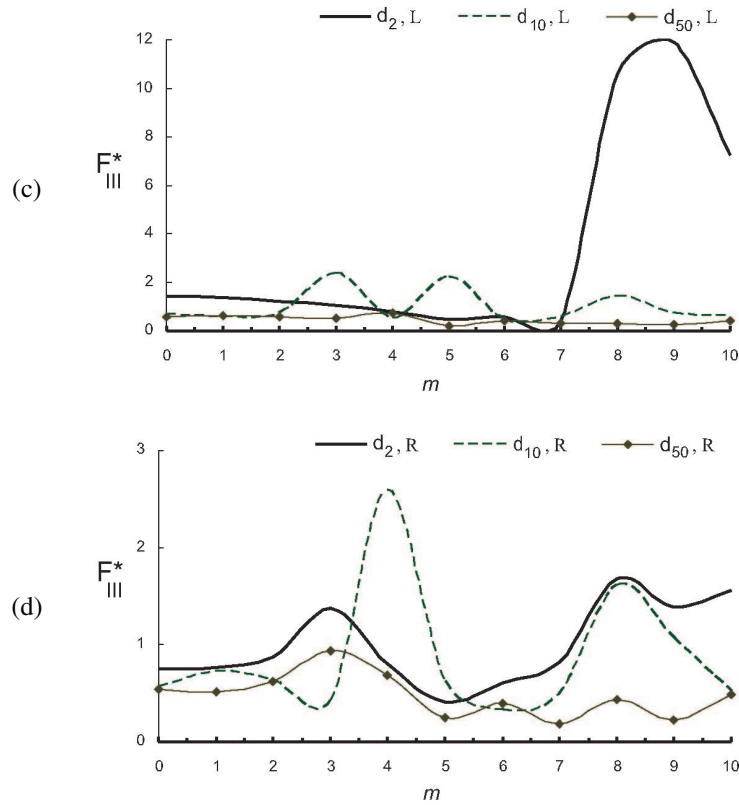


Fig. 4. Continued.

depth increases. For instance, at a depth of  $d_{50}$ , the SCF magnitudes are greatly reduced, as seen in Fig. 4;

- The incident wave angles that provoke SCF peaks depend strongly on the embedded depth, the observer's position (left or right crack-tip), and the type of crack (horizontal or vertical). Note that the results in Fig. 4 are based on fixed values for the inhomogeneity magnitude  $\beta = 0.2$ , the relief geometry, and the surface elasticity properties of both the nanorelief and the nanocrack.

The influence of the nanorelief shape on the development of local zones with non-uniform stress distribution is evident in Fig. 5.

Figure 5 shows the SCFs at the crack tips of horizontal and vertical nanocracks embedded at depth  $d = a + b$  in an exponentially graded half-plane with an inhomogeneity magnitude  $\beta = 0.2$ . The nanocracks are adjacent to a semi-elliptical nanocanyon with a major semi-axis  $a$  and varying minor axes  $b = 0.1a$ ,  $b = 0.5a$ ,

$b = a$ , under an SH-wave with a fixed frequency  $\Omega = 1.3$  and surface elasticity coefficients  $s_r = 0$  and  $s_{cr} = 0.02$ . The SCFs are plotted against the incident angle  $\theta = m\pi/20$ ,  $m = 0.0001, 1, \dots, 10$ . The geometry of the nanorelief strongly influences the stress concentration field, as seen in all figures. In most cases, the SCF magnitude is maximal when the nanocanyon has a horizontally elongated semi-elliptical shape, while a reduction in SCF is observed when the minor semi-axis is  $b = 0.5a$ . This pattern also depends on the incident wave angle, the type of the nanocrack, and the position of the crack tip. For vertical crack, the SCFs show much

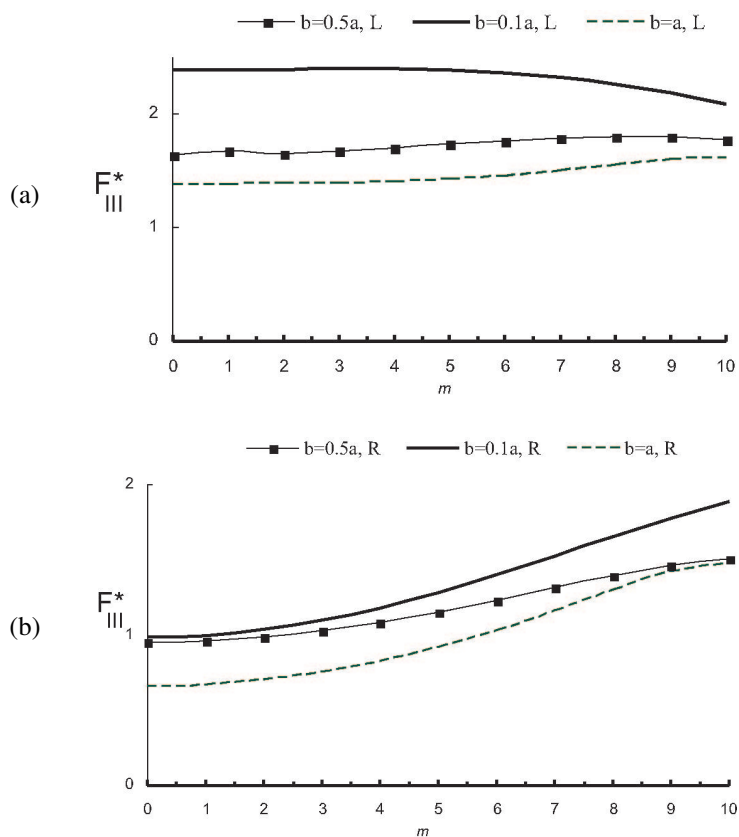


Fig. 5. Normalized SCF  $F_{III}^*$  at different crack-tips of a nanocrack embedded at depth  $d = a + b$  in an exponentially graded half-plane having semi-elliptical nanorelief  $\Gamma_{r_1}$  with major semi-axis  $a$  and different values of the minor axis  $b = 0.1a$ ,  $b = 0.5a$ ,  $b = a$  under SH-wave with frequency  $\Omega = 1.3$  and incident angle  $\theta = m\pi/20$ ,  $m = 0.0001, 1, \dots, 10$ : (a) left crack-tip L of a horizontal nanocrack; (b) right crack-tip R of a horizontal nanocrack; (c) left (upper) crack-tip L of a vertical nanocrack; (d) right (lower) crack-tip R of a vertical nanocrack.

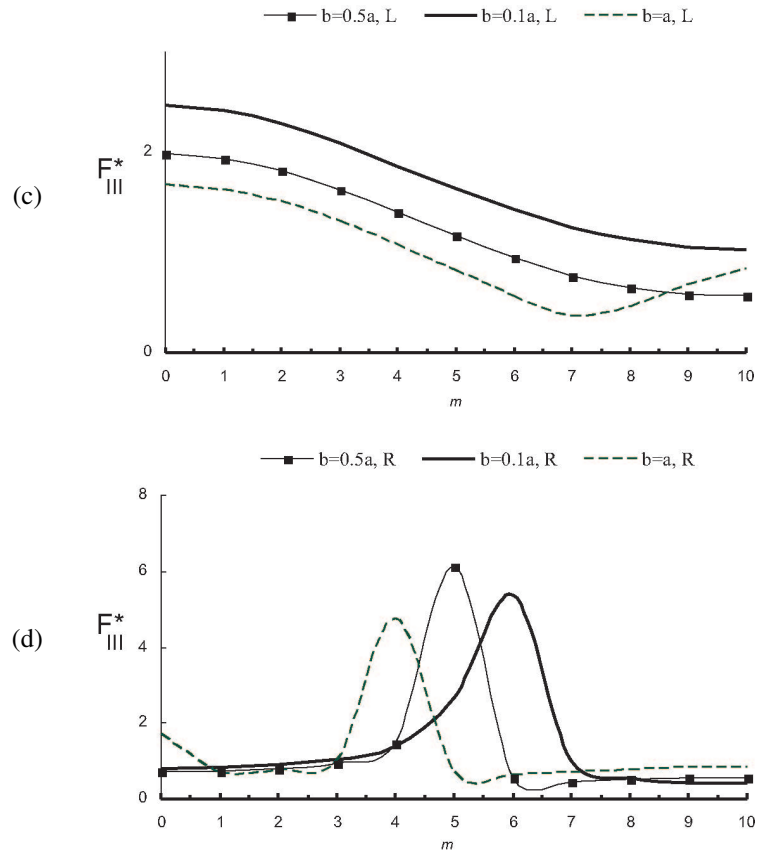


Fig. 5. Continued.

higher peak values compared to horizontal crack. This can be attributed to the direction of the material gradient, which aligns with the depth of the half-plane. Figure 5d demonstrates that the relief geometry significantly alters the incident angle at which the SCF reaches its peak. For example, when the nanorelief is semicircular, the SCF peak occurs at  $m = 4$  ( $36^\circ$ ), whereas for a horizontally elongated semi-elliptical geometry, the peak occurs at  $m = 6$  ( $54^\circ$ ).

The influence of the nanorelief surface elasticity  $s_r$  is shown in the results presented in Fig. 6, where the SCF  $F_{III}^*$  is plotted against the incident wave angle at different crack tips. The figures illustrate horizontal in Figs. 6a,b and vertical in Figs. 6c,d nanocrack embedded at a depth  $d = a + b$  for different values of  $s_r = 0; 0.002; 0.2$ , with all other model parameters fixed as specified in figure's caption.

Figure 6 reveals that there exists influence of the surface elasticity along the nanorelief and it is different for the nanocrack orientation-horizontal or vertical, and for different crack-tips positions. In the case of a horizontal crack the SCFs for  $s_r = 0.2$  are greater than in the case when surface elasticity is not taken into account. Just opposite is the situation in the case of a vertical crack. The influence of the incident angle value is much more expressive in the case of the vertical nanocrack, compare Fig. 6a and Fig. 6d. The role played by the nanorelief's surface elasticity is shown very clear in Fig. 6d, where in the presence of surface elasticity along the nanorelief, the SCF decreases significantly and this effect exists only when the wave propagation direction is defined by angle of  $m = 5$  ( $45^\circ$ ).

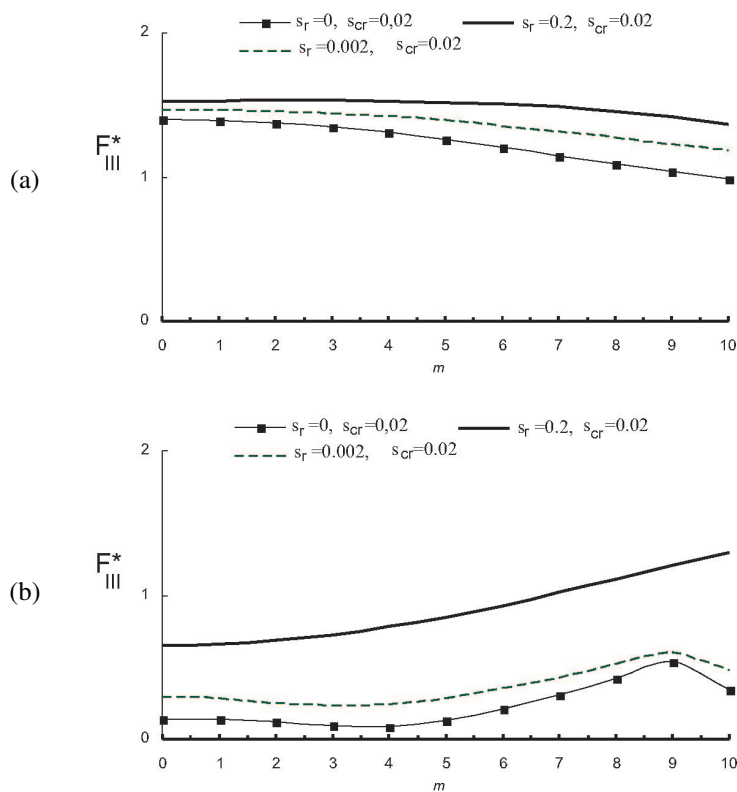


Fig. 6. Normalized SCF  $F_{III}^*$  at different crack-tips of a nanocrack embedded at depth  $d = a + b$  in an exponentially graded half-plane with inhomogeneity magnitude  $\beta = 0.2$  having semi-elliptic nanorelief  $\Gamma_{r_1}$  with major semi-axis  $a$  and the minor axis  $b = 0.5a$  under SH-wave with frequency  $\Omega = 1.3$  and incident angle  $\theta = m\pi/20$ ,  $m = 0.0001, 1, \dots, 10$ : (a) left crack-tip L of a horizontal nanocrack; (b) right crack-tip R of a horizontal nanocrack; (c) left (upper) crack-tip L of a vertical nanocrack; (d) right (lower) crack-tip R of a vertical nanocrack.

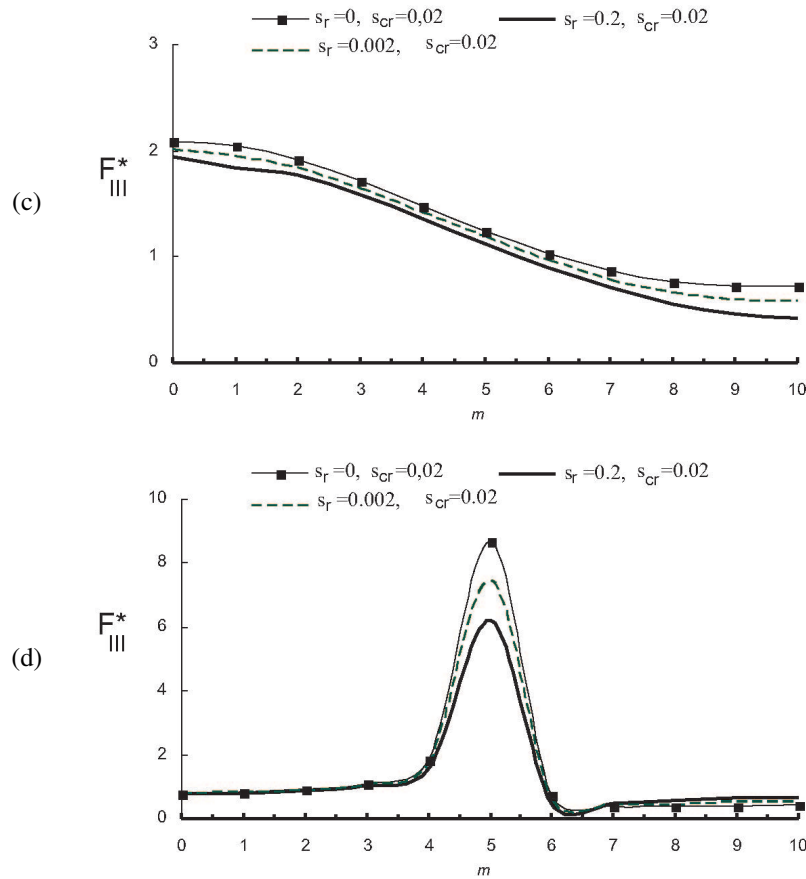


Fig. 6. Continued.

The influence of the nanocrack's surface elasticity  $s_{cr}$  is depicted in Fig. 7, which presents the SCF  $F_{III}^*$  as a function of the incident wave angle at various crack tips. The figures illustrate horizontal Fig. 7a,b and vertical Fig. 7c,d nanocrack embedded at a depth  $d = a + b$  for different values of  $s_{cr} = 0; 0.003; 0.02$ , while all other model parameters remain fixed, as specified in the figure's caption. This figure indicates that the surface elasticity of the nanocrack has a more pronounced effect on the SCFs than the surface elasticity properties of the nanorelief. Specifically, when  $s_{cr} \neq 0$ , the SCFs exhibit significantly higher values. The incident angle  $\theta$  corresponding to the SCF peaks varies for each case: (a)  $m = 0.0001$  for the left crack-tip of a horizontal nanocrack; (b)  $m = 10$  for the right crack-tip of a horizontal nanocrack; (c)  $m = 0.0001$  ( $0.0009^\circ$ ) for the upper crack-tip of a vertical nanocrack; (d)  $m = 5$  ( $45^\circ$ ) for the lower crack-tip of a vertical nanocrack.

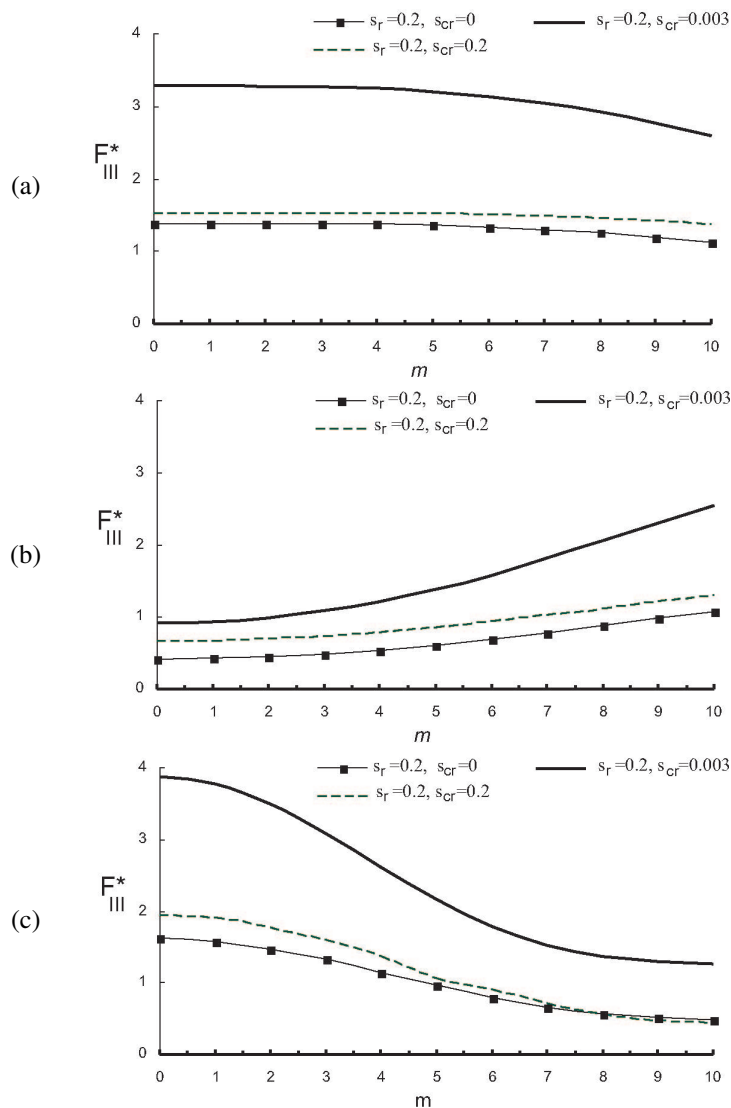


Fig. 7. Normalized SCF  $F_{III}^*$  at different crack-tips of a nanocrack embedded in an exponentially graded half-plane with semi-elliptic nanorelief  $\Gamma_{r_1}$  with major semi-axis  $a$  and minor axis  $b = 0.5a$  under SH-wave with frequency  $\Omega = 1.3$  and incident angle  $\theta = m\pi/20$ ,  $m = 0.0001, 1, \dots, 10$ : (a) left crack-tip L of a horizontal nanocrack; (b) right crack-tip R of a horizontal nanocrack; (c) left (upper) crack-tip L of a vertical nanocrack; (d) right (lower) crack-tip R of a vertical nanocrack.

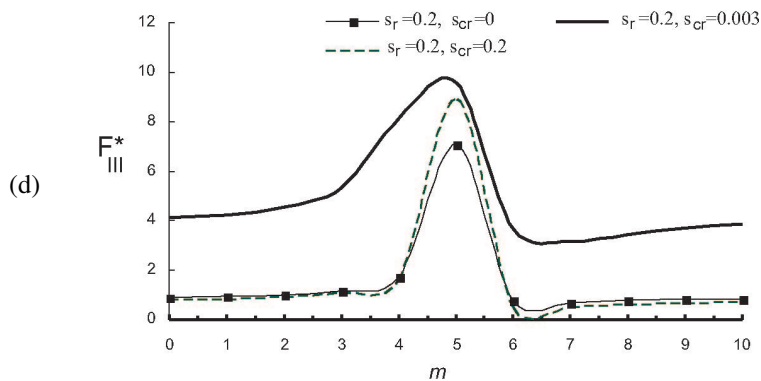


Fig. 7. Continued.

The influence of the material gradient is evident in the results shown in Fig. 8, which presents the SCF  $F_{III}^*$  as a function of the incident wave angle at various crack tips. This figure illustrates horizontal Fig. 8a,b and vertical Fig. 8c,d nanocracks embedded at a depth  $d = a + b$ , with different material gradient values  $\beta = 0; 0.2; 0.4$ , while all other model parameters remain fixed as specified below the figure. Figure 8 reveals that increasing the material gradient generally leads to a decrease in SCF amplitudes in cases of Fig. 8a,b,c. However, in case of Fig. 8d, corresponding to

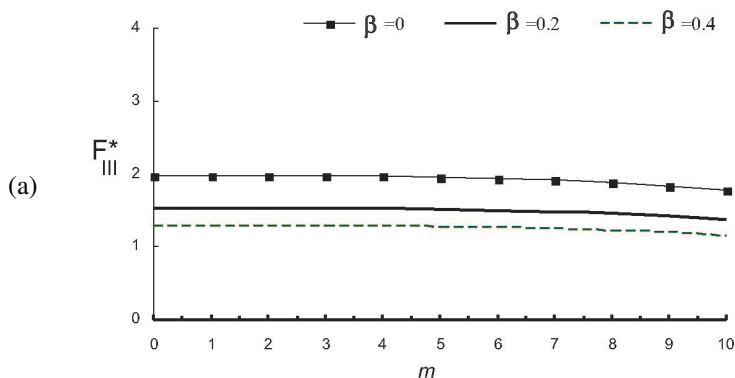


Fig. 8. Normalized SCF  $F_{III}^*$  at different crack-tips of a nanocrack embedded in an exponentially graded half-plane with  $\beta = 0.0001; 0.2; 0.4$  and having semi-elliptical nanorelief  $\Gamma_{r_1}$  with major semi-axis  $a$  and  $b = 0.5a$  under SH-wave with frequency  $\Omega = 1.3$  and incident angle  $\theta = \frac{m\pi}{20}$ ,  $m = 0.0001, 1, \dots, 10$ : (a) left crack-tip L of a horizontal nanocrack; (b) right crack-tip R of a horizontal nanocrack; (c) left (upper) crack-tip L of a vertical nanocrack; (d) right (lower) crack-tip R of a vertical nanocrack. Surface elasticity coefficients of the nanorelief is  $s_r = 0.2$  and of the nanocrack is  $s_{cr} = 0.02$ .

the lower crack tip of a vertical nanocrack, the trend is reversed. Additionally, the incident angle  $\theta$  corresponding to the SCF peaks varies across the cases and aligns with the tendencies observed in Fig. 7.

The last set of results concerns a graded cracked piezoelectric half-plane with a

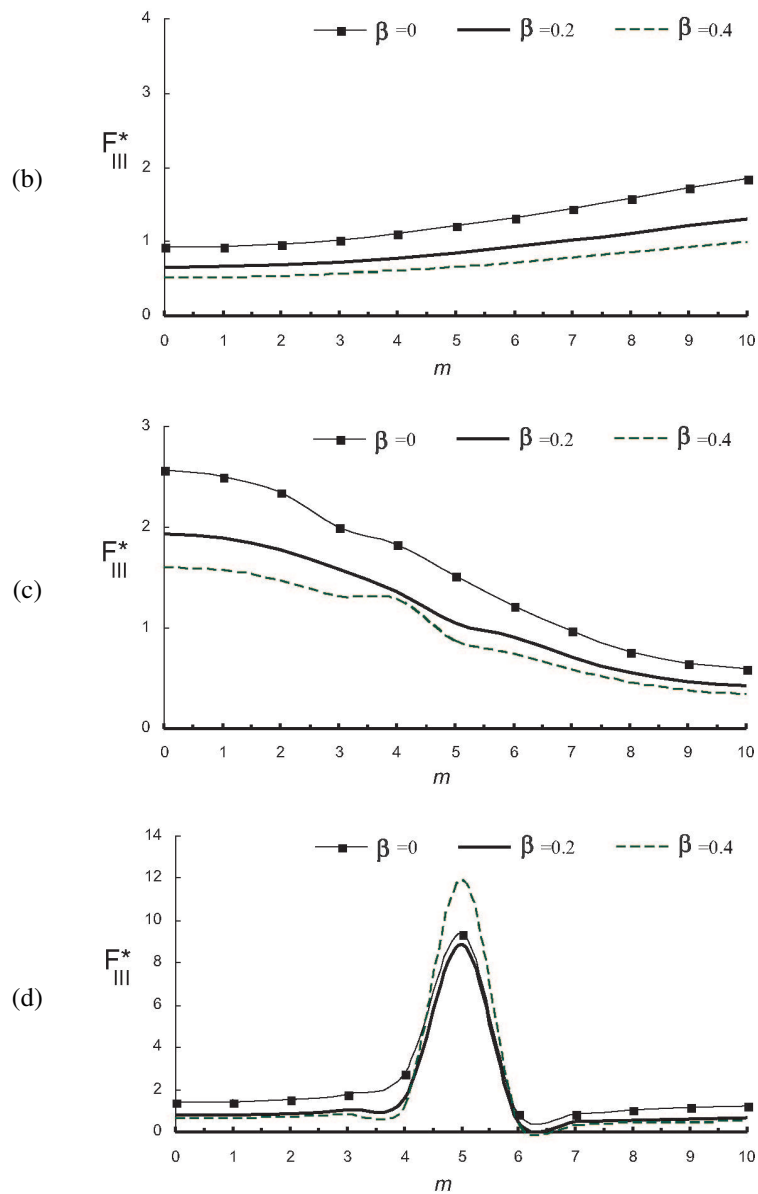


Fig. 8. Continued.

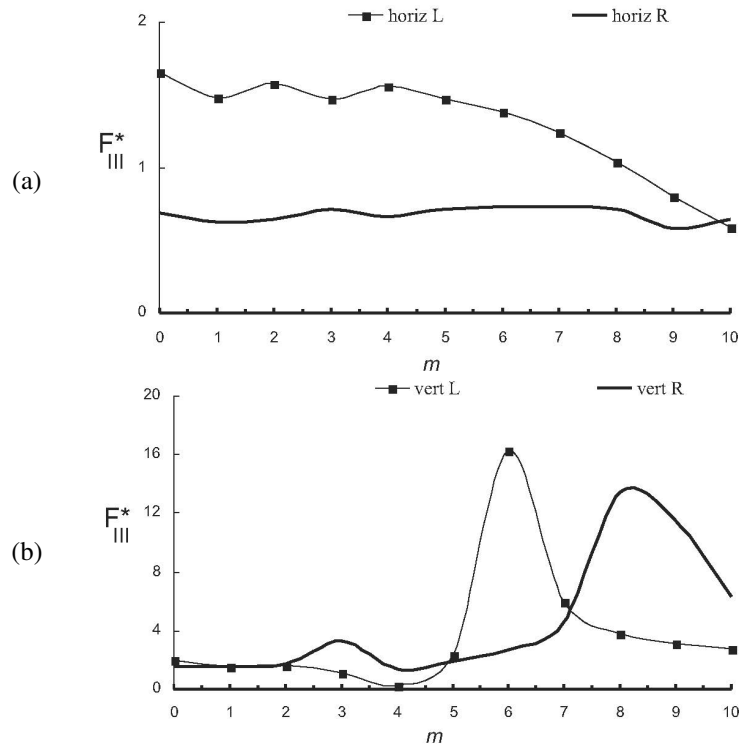


Fig. 9. Normalized SCF  $F_{III}^*$  at observer points L, R of an embedded nanocrack at depth  $d = a + b$  in a graded half-plane with a wave relief profile along its surface  $\Gamma_{r_2}$  with  $b = a$ , see Fig 1b, under SH-wave with frequency  $\Omega = 1.3$  and incident angle  $\theta = \frac{m\pi}{20}$ ,  $m = 0.0001, 1, \dots, 10$ . The obtained results are for: (a) horizontal crack - left crack-tip L and right crack-tip R; (b) vertical crack - left crack-tip L and right crack-tip R.

nanorelief in the form of a wave profile along its surface, see Fig. 1b. Normalized mechanical SCF  $F_{III}^*$  at the crack-tips L and R of an embedded horizontal or vertical nanocrack are plotted in Figs. 9, 10 as functions of the incident angle  $\theta$  of a propagating elastic SH wave with a fixed frequency  $\Omega = 1.3$ . The fixed model parameters in Fig. 9 are as follows:  $\beta = 0.0001$ ,  $s_r = 0$ , and  $s_{cr} = 0.02$ , while those in Fig. 10 are:  $\beta = 0.2$ ,  $s_r = 0.002$ , and  $s_{cr} = 0.02$ . Both figures reveal the following effects:

- The type and geometry of the relief, both with and without surface elasticity properties, have a strong influence on the stress concentration fields near the crack tips of both types of nanocracks. This conclusion holds true for both homogeneous and graded continua. This effect is evident when comparing results for a half-plane with a nanorelief on its surface versus one with a relief in the form of a wave profile;

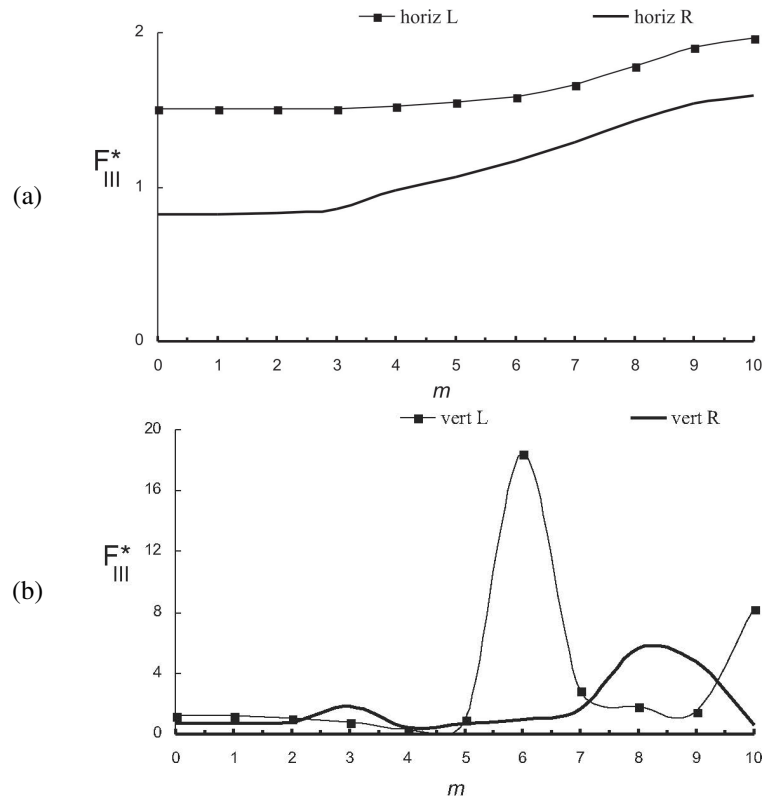


Fig. 10. Normalized SCF  $F_{III}^*$  at observer points L, R of an embedded nanocrack crack at depth  $d = a + b$  in a graded half-plane with a wave relief profile along its surface  $\Gamma_{r_2}$  with  $b = a$ , see Fig 1b, under SH-wave with frequency  $\Omega = 1.3$  and incident angle  $\theta = m\pi/20$ ,  $m = 0.0001, 1, \dots, 10$ . The obtained results are: (a) horizontal crack – left crack-tip L and right crack-tip R; (b) vertical crack – left crack-tip L and right crack-tip R.

- The presence of a material gradient alters the SCFs at both crack tips of the horizontal nanocrack, depending on the wave propagation direction. In the case of a homogeneous material, the maximum values occur at  $m = 0.0001$  ( $0.0009^\circ$ ). However, for a graded material profile with  $\beta = 0.2$ , the maximum SCFs shift to  $m = 10$  ( $90^\circ$ ). For the vertical nanocrack, the lower crack tip retains its peak at  $m = 6$  ( $54^\circ$ ), while the upper crack tip reaches its maximum at approximately  $m = 8$  ( $72^\circ$ ), but in the presence of a material gradient, its corresponding peak is reduced;
- The stress concentration zones around the vertical nanocrack are significantly higher than those around the horizontal crack, regardless of the fixed model parameters;

- The results from these figures confirm the general conclusion that SCFs vary significantly and depend on several factors: the nanorelief and nanocrack type and their surface elasticity, the presence and magnitude of the material gradient, the crack-tip location, and the properties of the incident wave.

The simulations conducted in this study demonstrate that the non-uniform distribution of dynamic stress and electrical fields is influenced by several key factors:

- the characteristics of the incident wave;
- the geometry of the crack configuration within the graded half-plane boundary;
- the magnitude of the material gradient;
- the reference material properties;
- the coupled material properties of piezoelectric composites;
- the surface elasticity effects of nano-objects,
- the type of the nanorelief,
- the ratio of wavelength to crack length.

The strong size-effect of nanocracks and nanorelief significantly impacts the dynamic fracture behavior of piezoelectric solids, which can greatly influence their overall reliability. The results clearly demonstrate that piezoelectric solids containing nanoscale cracks, nanorelief peculiarities and surface features exhibit unique fracture behavior, distinctly different from their macroscale counterparts.

## 5 CONCLUSION

This study examines the 2D anti-plane dynamic response of a piezoelectric inhomogeneous half-plane at the nanoscale, containing an embedded nanocrack and a nanorelief along its boundary, subjected to elastic SH waves. The analysis employs the BIEM based on the half-plane Green's function. The BIEM is tailored for a specific type of inhomogeneity in one principal direction of the matrix material, referred to as the depth coordinate, where material parameters vary exponentially. The BIEM provides an exact formulation for the response of a nano-crack in a graded half-plane with a relief, with approximations arising solely from discretizing the nanocrack and nanorelief surface. The numerical solution is verified against benchmark case from the literature and subsequently applied to simulations that reveal the detailed behavior of the nanocrack and its surrounding matrix material. The methodology presented

is effective for predicting both kinematic and stress fields near nanocracks in inhomogeneous matrices with internal nanorelief, offering valuable insights for the design of nanoscale components.

The numerical simulations reveal that the stress concentration field near the crack arises from a complex interplay of several key factors. These include the frequency content and propagation direction of the elastic wave, the magnitude of the material gradient, surface elasticity effects, size factor, the geometric configuration of the nanocrack, coupled electro-elastic fields, and the dynamic interaction between the crack, canyon, and half-plane boundary. The novelty of this work lies in the effective integration of four key stages of analytical and numerical development:

- (a) mechanical modeling grounded in classical continuum mechanics theory for the bulk solid under dynamic load;
- (b) incorporation of non-classical boundary conditions derived from localized constitutive equations at nano-material interfaces;
- (c) efficient numerical implementation utilizing the analytically derived graded half-plane Green's function, and
- (d) low computational cost, achieved by restricting numerical modeling to the surfaces of the embedded nanocrack.

The systematic development of nanomechanical models remains an ongoing effort, primarily because achieving this goal requires multidisciplinary expertise spanning continuum mechanics, computational mechanics, materials science, mathematical physics, chemistry, and physics. In this context, the results obtained in this study including a comprehensive package of a mechanical model, an efficient computational methodology, verified proprietary software, and parametric simulations—are both valuable and timely contributions to the field of nanomechanics.

#### ACKNOWLEDGEMENT

This work is partially supported by the Bulgarian National Science Fund, contract No KII-06-H57/3/15.11.2021.

APPENDIX

FREE FIELD MOTION

We start with the incident generalized displacement solution  $u_K^{\text{in}} = h^{-1/2}(x)U_K^{\text{in}}$ . Vector function  $U^{\text{in}} = \begin{Bmatrix} U_3^{\text{in}} \\ U_4^{\text{in}} \end{Bmatrix}$  is obtained by the wave decomposition method, following Chapter 11 in [13], which is expressed as follows:

$$U^{\text{in}} = \begin{pmatrix} 1 \\ e_{15}^0/\varepsilon_{11}^0 \end{pmatrix} e^{ik(x_1\zeta_1+x_2\zeta_2)},$$

where  $\zeta_1 = \cos \theta$ ,  $\zeta_2 = \sin \theta$  and  $\theta \in (0, \pi/2]$  is the direction of the SH wave. Then we are asking the free-field wave solution in the form

$$u_K^{\text{ff}} = h^{-1/2}(x) (A_1U_K^{\text{in}} + A_2U_K^{\text{sc}}),$$

where  $U^{\text{in}}$  is defined above and

$$U^{\text{sc}} = \begin{pmatrix} 1 \\ e_{15}^0/\varepsilon_{11}^0 \end{pmatrix} e^{ik(x_1\zeta_1-x_2\zeta_2)}.$$

Our aim is to determine constants  $A_1, A_2$  such that the boundary condition (3) holds. Note that the amplitude of the incident wave is usually assumed to be unit,

$$\begin{pmatrix} u_3^{\text{ff}} \\ u_4^{\text{ff}} \end{pmatrix} = e^{-ax_2} \begin{pmatrix} 1 \\ e_{15}^0/\varepsilon_{11}^0 \end{pmatrix} \left[ A_1e^{-ik(x_1\zeta_1+x_2\zeta_2)} + A_2e^{-ik(x_1\zeta_1-x_2\zeta_2)} \right].$$

After some simplifications we obtain that boundary conditions  $T_3^{u^{\text{ff}}}|_{x_2=0} = 0$ , and  $T_4^{u^{\text{ff}}}|_{x_2=0} = 0$  are satisfy if  $A_2 = \frac{a_2 + ik\zeta_2}{-a_2 + ik\zeta_2} A_1$ .

GREEN'S FUNCTION

The Green function is a fundamental solution that satisfies in addition the prescribed traction-free boundary condition (3) on the boundary  $\Gamma_{\text{ff}} = \{x : x_2 = 0\}$ , i.e.,  $g(x, \xi, \omega)$  is defined as solution of the problem

$$\begin{cases} \sigma_{iJM,i}^g + \rho_{JK}\omega^2 g_{KM} = \delta_{JM}\delta(x, \xi), & x, \xi \in \mathbb{R}_-^2 \\ t_{JM}^g = 0 & \text{on } x_2 = 0, \end{cases}$$

where  $\delta(x, \xi)$  is Dirac's delta function,  $\delta_{JM}$  is Kroneker symbol, the stress is  $\sigma_{iJM}^g = C_{iJKl}g_{KM,l}$ , the traction on  $x_2 = 0$  is  $t_{JM}^g = \sigma_{iJM}^g n_i$ ,  $n = (0, 1)$ .

Let us introduce the notations

$$M^0 = \begin{pmatrix} 1 & e_{15}^0/\varepsilon_{11}^0 \\ e_{15}^0/\varepsilon_{11}^0 & (e_{15}^0/\varepsilon_{11}^0)^2 \end{pmatrix}, \quad N^0 = \begin{pmatrix} 0 & 0 \\ 0 & 1/\varepsilon_{11}^0 \end{pmatrix}.$$

We start with the fundamental solution of Eq. (1) with Dirac’s delta function on the right hand side is a  $2 \times 2$  matrix-valued function

$$u^*(x, \xi, \omega) = -e^{-a_2(x_2+\xi_2)} \left[ \frac{i}{4\gamma} M^0 H_0^{(1)}(kr(x, \xi)) + \frac{1}{4} N^0 H_0^{(1)}(i|a_2|r(x, \xi)) \right],$$

where  $H_0^{(1)}$  is Hankel function of the first kind and 0-th order and the distance between the source and observer points is  $r(x, \xi) = \sqrt{(x_1 - \xi_1)^2 + (x_2 - \xi_2)^2}$ .

In order to obtain analytically the half-plane Green’s function we are asking for a correction term  $w(x, \xi, \omega)$  that satisfies the Eq. (3) and such that

$$g(x, \xi, \omega) = u^*(x, \xi, \omega) + w(x, \xi, \omega)$$

satisfies the traction-free boundary condition, i.e.,  $t_{JM}^g = t_{JM}^{u^*} + t_{JM}^w = 0$  on  $x_2 = 0$  holds.

Using the representation of Hankel function, see [14], presented as an inverse Fourier transform with respect to  $x_1$ , we can find the elements of the matrix-valued function  $w(x, \xi, \omega)$  presented in the original domain as

$$w_{IJ}(x, \xi, \omega) = e^{-ax_2} W_{IJ}(x, \xi, \omega),$$

where the matrix-valued function in the transformed domain is

$$W_{IJ} = e^{-a_2\xi_2} \int_{\mathbb{R}} \left( S_{IJ} \frac{1}{\tau} e^{\tau(x_2+\xi_2)} + D_{IJ} \frac{1}{\tau_a} e^{\tau_a(x_2+\xi_2)} \right) e^{i\eta(x_1+\xi_1)} d\eta.$$

Here  $\tau = \sqrt{\eta^2 - k^2}$  and  $\tau_a = \sqrt{\eta^2 + a_2^2}$ . Coefficients  $S_{IJ}$ ,  $D_{IJ}$  are found by the satisfaction of the traction-free boundary condition for  $g(x, \xi, \omega)$  and are presented below

$$S_{33} = \frac{1}{4\pi\gamma} \frac{\tau + a_2}{\tau - a_2}, \quad S_{43} = \frac{e_{15}^0}{\varepsilon_{11}^0} S_{33}, \quad S_{34} = \frac{e_{15}^0}{\varepsilon_{11}^0} \frac{1}{4\pi\gamma} \frac{\tau + a_2}{\tau - a_2}, \quad S_{44} = \frac{e_{15}^0}{\varepsilon_{11}^0} S_{34},$$

$$D_{33} = D_{34} = D_{43} = 0, \quad D_{44} = \frac{e_{15}^0}{\varepsilon_{11}^0} \frac{1}{4\pi} \frac{\tau_a + a_2}{\tau_a - a_2}.$$

Three types of solutions are possible, namely the first for frequencies higher than the defined critical frequency  $\omega_{cr} = |a_2|\sqrt{\gamma/\rho^0}$ , where the dynamic behaviour is

described by a wave propagation process, the second is for frequencies equal to the critical frequency describing the static behaviour and lower than the defined critical frequency, where only simple vibrations occurs. In this study is considered the case of a wave propagation process.

Both free-field wave motion solution and Green's function for an exponentially graded in depth piezoelectric half-plane depend on the wave frequency, reference coupled material properties and magnitude of the material gradient.

#### REFERENCES

- [1] J. OGILVY (1991) "Theory of Wave Scattering from Random Rough Surfaces". CRC Press, New York.
- [2] R. AGRAWAL, B. PENG, E. GDOUTOS, H. ESPINOSA (2008) Elasticity size effects in zno nanowires—a combined experimental-computational approach. *Nano Letters* **8**(11) 3668-3674.
- [3] F. XU, Q. QIN, A. MISHRA, Y. GU, Y. ZHU (2010) Mechanical properties of ZnO nanowires under different loading modes. *Nano Research* **3** 271-280.
- [4] M. MINARY-JOLANDAN, R.A. BERNAL, I. KULJANISHVILI, V. PARPOIL, H. D. ESPINOSA (2012) Individual GaN nanowires exhibit strong piezoelectricity in 3D. *Nano Letters* **12**(2) 970-976.
- [5] G.D. MANOLIS, P.S. DINEVA, T. RANGELOV, D. SFYRIS (2021) Mechanical models and numerical simulations in nanomechanics: a review across the scales. *Engineering Analysis with Boundary Elements* **128** 149-170.
- [6] M.E. GURTIN, A.I. MURDOCH (1975) A continuum theory of elastic material surfaces. *Archive for Rational Mechanics and Analysis* **57** 291-323.
- [7] T. RANGELOV, P. DINEVA (2017) Dynamic fracture behaviour of a nanocrack in a piezoelectric plane. *ZAMM* **97**(4) 1393-1405.
- [8] P. DINEVA, M. MARINOV, T. RANGELOV (2019) Dynamic fracture of a nano-cracked finite exponentially inhomogeneous piezoelectric solid. *Archive of Applied Mechanics* **99**(7) 1317-1332.
- [9] T. RANGELOV, Y. STOYNOV, P. DINEVA (2022) Dynamic nanocracks interaction in graded magnetoelastoelectric solid. *Journal of Theoretical and Applied Mechanics* **52** 335-351.
- [10] G. MANOLIS, G. DADOULIS, P. DINEVA, T. RANGELOV (2024) Green's functions for the viscoelastic halfspace: A convolutional neural network approach. *Journal of Theoretical and Applied Mechanics* **54**(4) 375-390.
- [11] S. PARVANOV, P. DINEVA (2024) Wave scattering by nanoinclusions in anisotropic plane. Part 1: Mechanical model and computational methodology. *Journal of Theoretical and Applied Mechanics* **54**(2) 186-200.
- [12] S. PARVANOV, P. DINEVA (2024) Wave scattering by nanoinclusions in anisotropic plane. Part 2: Parametric study. *Journal of Theoretical and Applied Mechanics* **54**(2) 201-215.

- [13] P. DINEVA, D. GROSS, R. MÜLLER, T. RANGELOV (2014) “Dynamic Fracture of Piezoelectric Materials. Solutions of Time-harmonic problems via BIEM. Solid Mechanics and its Applications”, v. 212. Springer Int. Publ., Switzerland.
- [14] I.S. GRADSHTEYN, I.M. RYZHIK (1965) “Tables of Integrals, Series, and Products”. Academic Press, New York.
- [15] T. RANGELOV, P. DINEVA (2023) Green’s function and wave scattering in inhomogeneous anti-plane pem half-plane. In: A. Slavova, editor, “NTADES 2022, Springer PROMS, v. 412”, pp. 117-127, Springer Nature.
- [16] R.E. MILLER, V.B. SHENOY (2000) Size-dependent elastic properties of nanosized structural elements. *Nanotechnology* **11**(1) 39-47.
- [17] WOLFRAM RESEARCH (2007) “Mathematica 6.0 for MS Windows” Champaign, Illinois.
- [18] X.D. WANG, S.A. MEGUID (2000) Effect of electromechanical coupling on the dynamic interaction of cracks in piezoelectric materials *Acta Mechanica* **143** 1-15.
- [19] G.D. MANOLIS, T.V. RANGELOV, P.S. DINEVA (2024) Chapter 5: The inhomogeneous half-plane with surface elasticity effects under dynamic loads. In: K.K. Žur and S A. Faghidian, editors, “Nanomechanics of Structures and Materials. Modeling and Analysis”, pp. 133-179, Elsevier.